Analytical Methods

ROYAL SOCIETY OF CHEMISTRY

PAPER

View Article Online
View Journal

Cite this: DOI: 10.1039/d0ay01398f

Molybdenum disulfide@5-carboxyfluorescein-probe biosensor for unamplified specific fragment detection in long nucleic acids based on magnetic composite probe-actuated deblocking of secondary structure†

Bin Guo,‡[ab] Yurong Yan,‡[a] Lu Fan,[a] Haiping Wu,[a] Min Zhao,[a] Xiaolei Duan,[a] Wei Cheng[c] and Shijia Ding*[a]

Received 21st July 2020
Accepted 7th September 2020

DOI: 10.1039/d0ay01398f

rsc.li/methods

Secondary structures in long circulating tumor nucleic acids have potential obstacles for specific location point hybridized detection of gene fragments. The exploration of biosensing strategies requires selectively changing the nucleic acids conformation and inducing signal switching. Herein, a self-assembled magnetic composite probe (MCP) was fabricated by the hybridization reaction of Linker DNA and a "Y"-junction-DNA nanostructure on the surface of magnetic beads, contributing to the capture, secondary structure unlocking, and enrichment of the PML/RARα DNA "L" subtype. Then, by integrating the MCP-actuated reactor, a one-step "off–on" signal switching MoS_2@FAM-probe biosensing method was developed for the efficient detection of the PML/RARα DNA "L" subtype. The proposed biosensor was capable of detecting 100 bases PML/RARα DNA "L" subtype with a wide linear range of 1 pM to 200 nM and a limit of detection down to 0.223 pM without signal amplification. In addition, the biosensing method was successfully applied for the detection of target in serum samples. It is worth pointing out that this simple biosensing strategy could enable long nucleic acids fragments with secondary structures from ctDNA and ctRNA to be quantitatively assayed based on direct hybridization.

1. Introduction

The plentiful research on long nucleic acids has given us multifaceted knowledge of their intricate structure and function. For example, the long non-coding RNA was found to take part in the interaction of various proteins, RNA, and DNA in regulating the expression of gene at different transcriptional levels.[1,2] Moreover, recent literature reports provide evidence to postulate the consequential role of long nucleic acids as carrier of more gene mutation or fusion information.[3] Thus, the analysis of long cell-free nucleic acids would offer new opportunities for the assessment of relevant diseases progress in the field of molecular diagnosis.[4]

At present, many vital biosensing methods based on direct hybridization have been developed and applied in the detection of target genes, in which an oligonucleotide probe has specific recognition and binds to its complementary target,[5] including the L858R mutation occurring in the Epidermal Growth Factor Receptor (EGFR) gene and the PML/RARα DNA fusion gene. However, only direct hybridization methods are capable of detecting nucleic acids with a sequence length of up to 40 bases without signal amplification;[6,7] whereas the average size of the cell-free L858R mutation gene and PML/RARα gene is about 130 bases in length,[8,9] and these longer nucleic acids present severe problems for detection, making direct hybridization detection more difficult. For example, the long sequence PML/RARα gene can form thermodynamically stable secondary structures, which impede the crosslinking between the specific target fragment and probe. Correspondingly, the L858R mutant site can be buried in stem loop structures from long sequences, which can also affect the detection efficiency.[10,11] In addition, the present assays face several other technical challenges arising from low concentration of cell-free nucleic acids and interference of the matrix on the analysis system, which greatly reduces the accuracy of detection results.[12] Therefore, there is a crucial need to perform an in-depth investigation into the

[a]Key Laboratory of Clinical Laboratory Diagnostics (Ministry of Education), College of Laboratory Medicine, Chongqing Medical University, Chongqing 400016, China. E-mail: dingshijia@cqmu.edu.cn; dingshijia@163.com; Fax: +86-23-68485786; Tel: +86-23-68485688

[b]Department of Clinical Laboratory, The Affiliated Hospital of North Sichuan Medical College, Nanchong 637000, China

[c]The Center for Clinical Molecular Medical Detection, The First Affiliated Hospital of Chongqing Medical University, Chongqing 400016, China

† Electronic supplementary information (ESI) available. See DOI: 10.1039/d0ay01398f

‡ These authors contributed equally to this work.

detection of long nucleic acids with secondary structures in complex matrices.

Over the past few years, DNA self-assembly has been utilized to fabricate various nanostructures by employing programmed DNA as building units,[13] including DNA tiles,[14] DNA dendrimers,[15] DNA tetrahedrons,[16] DNA nanotweezers,[17] and DNA hydrogels.[18] Moreover, several classes of DNA nanostructures can serve as molecular probes for biosensing applications.[19] For example, Chen *et al.* reported a rationally designed double-stranded probe with forked single-stranded overhangs (Y-junction-structure), which exhibited reliable and efficient performance for the detection of individual base pair changes in long double-stranded DNA.[20] However, the homogeneous methods are susceptible to the interference of the endogenous matrix in the sample during the detection process.[21] Therefore, to solve this problem, magnetic composite extraction materials (MCEM) have been widely used for the extraction of a variety of nucleic acids and protein molecules.[22] For example, Xing *et al.* reported an enrichment and analysis method based on a reduced graphene oxide-based magnetic material, which could achieve the ultrasensitive detection of miRNA.[23] Interestingly, a novel multifunctional nano-conjugate probe could be assembled by a "Y"-junction-nanostructure ("Y"-Capture Probe, "Y"-CP) and magnetic composite materials, which might play an important role in the detection of long nucleic acids.

Förster resonance energy transfer (FRET) pairs consist of a fluorophore and a quencher. Based on the distance between a FRET pair, the fluorescence occurs upon conversion between quenching and recovery, and can be coupled with a biomolecular recognition process.[24] Molybdenum disulfide (MoS_2) nanosheets contain three atomic layers as S–Mo–S metal layers, which are covalently bonded with each other.[25,26] As one of the fluorescence quenchers in FRET, MoS_2 nanosheets can adsorb 5-carboxyfluorescein (FAM)-labeled single-stranded DNA (ssDNA) by the van der Waals force between the nucleobases and the basal plane of MoS_2. Then, the fluorescence of FAM is quenched because the emission spectrum of the FAM molecule overlaps with the absorption spectrum of the MoS_2 nanosheets. On the contrary, after the target hybridizates with its complementary FAM-probe, due to the nucleobases being covered between the densely negatively charged helical phosphate backbones, the MoS_2 nanosheets cannot adsorb double-stranded DNA (dsDNA), meaning that the FAM-labeled probe separates from the MoS_2 nanosheets, resulting in a recovery of the fluorescence signal.[27,28] Thus, the MoS_2 nanosheets-FAM pair is suitable for the fabrication of efficient biosensors.[29,30] For instance, Gao's group reported a simple detection method for DNA methyltransferase activity by using MoS_2 nanosheets as an effective fluorescence quencher.[31] Fu's group proposed a sensitive and quick detection strategy utilizing uranyl ions based on the fluorescence quenching of MoS_2 nanosheets and specific DNAzyme.[32] Also, MoS_2 nanosheets have the advantages of low price and simple preparation. Thus, these results demonstrate that MoS_2 nanosheets are a good candidate as a biosensing interface for potential applications in "off–on" fluorescence signal switching.

Here, we report a new method for long PML/RARα DNA detection based on a MoS_2@FAM-probe biosensing strategy in combination with the magnetic composite probe (MCP)-actuated recognition and extraction of a target. Initially, the smart "Y"-CP is the key element responsible for specifically capturing and unlocking the fusion site by triggering a conformation change in the nucleic acids. Next, the MoS_2@FAM-probe biosensor can achieve "off–on" fluorescence signal switching through a one-step hybridization. Using the long PML/RARα DNA "L" subtype as the model analyte,[33,34] the developed fluorescence method achieved the facile and sensitive specific fragment detection of 100 bases sequence without intricate amplification, which is a breakthrough in the detection of long nucleic acids with secondary structures. Furthermore, the serum samples of PML/RARα DNA could be successfully identified by this assay. Thus, the biosensing strategy presents a promising platform for the direct hybridization detection of complex long nucleic acids in clinical biochemical analysis, such as circulating tumor DNA and RNA (ctDNA, ctRNA).

2. Materials and methods

2.1. Materials and reagents

BioMag® Carboxyl as magnetic beads (MBs, 20 mg mL^{-1}) was purchased from Bangs Laboratories, Inc. (Indiana, U.S.A.). Bulk MoS_2 powders and salmon sperm DNA were brought from Sigma-Aldrich Chemical Co. (St. Louis, MO, U.S.A.). FAM, dimethyl sulfoxide, DL500 DNA Marker was purchased from TaKaRa Biotech (Dalian, China). Agarose was purchased from Sangon Inc. (Shanghai, China). Fetal bovine serum was purchased from Thermo Fisher Scientific (Massachusetts, USA). All the oligonucleotides were synthesized by Sangon Inc. (Shanghai, China) and the nucleic acid chains are listed in Table S1 (ESI†). Also, 0.1 M imidazole buffer (pH 7.0) containing 8.22 mL of 1-methylimidazole and 900 mL of DEPC-treated deionized water were used as the amide reaction solution.

2.2. Apparatus

The UV-vis absorption spectrum was recorded with a UV-2550 UV-visible spectrophotometer (Shimadzu, Japan). The fluorescence spectra were obtained by using a Cary Eclipse Fluorescence Spectrophotometer (Agilent Technologies, USA). Gel electrophoresis was carried out using a DYY-6C electrophoresis analyzer (Liuyi Instrument Company, China), and the imaging was performed with Bio-rad ChemDoc XRS (Bio-Rad, USA). Atomic force microscopy (AFM) (Bruker AXS, Germany), scanning electron microscopy (SEM) (FeiNa. Phenom. Prox, Netherlands), and transmission electron microscopy (TEM) (Hitachi H7500, Japan) were employed to characterize the thickness, size, and morphology of the MoS_2 nanosheets. Circular dichroism (CD) spectra were recorded on a chirascan spectropolarimeter (Applied Photophysics Ltd, UK). Image lab 3.0 was used to analyse the gray-scale values of the electrophoresis band.

2.3. Synthesis of the MoS_2 nanosheets

MoS_2 nanosheets were synthesized as per the reported work with minor modification as follows. First, 30 mg of MoS_2 powders was added into a 25 mL flask. Then, 10 mL ethanol–water (45%, v/v) used as the dispersion solvent was added into the same flask. This was followed by continuous ultrasonication for 8 h, and then the dispersion was centrifuged at 4000 rpm for 20 min to collect the supernatant.[35] The MoS_2 nanosheets dispersion was characterized by using an UV-vis spectrophotometer (wavelength range from 300 to 800 nm), AFM, SEM, and TEM, and stored at 4 °C.

2.4. Preparation of the MB@Linker DNA (magnetic bead probe, MBP) and the magnetic composite probe

First, 10 μL of MBs and 200 μL of DEPC-treated water were transferred into a reaction flask. Then, the resultant mixture was shook vigorously and separated magnetically until the supernatant was clear, followed by aspirating the supernatant and leaving the MBs as a wet cake on the container wall (repeat three times). Second, 38.4 mg of EDC was added into 1 mL of 0.1 M imidazole buffer as the coupling agent, and the resultant mixture was gentle shook until complete dissolution occurred. Next, 200 μL of 10 nM of amine-terminated oligonucleotide (Linker DNA) was transferred into the 1 mL of EDC solution and mixed well; followed by adding the oligonucleotide/EDC solution from the above section to the washed MBs and rotating gently for 24 h at room temperature. Finally, the supernatant was separated magnetically and aspirated to remove the unreacted Linker DNA as well as the coupling agent. The resulting MBPs were then rinsed three times with DEPC-treated water following the above protocol, and re-suspended in a final volume of 500 μL of hybridization buffer and stored at 4 °C for further usage.

To obtain the MCPs, first 100 μL of 1 μM RARα-probe and 100 μL of 1 μM PML-probe were mixed together. Then, the mixture was annealed to form the desired "Y"-CP with a 500 nM concentration according to the following heating process: 90 °C, 5 min; 70 °C, 40 min; 50 °C, 40 min; 30 °C, 40 min; 20 °C, 40 min; 10 °C, 40 min; and 4 °C, 24 h. Second, 100 μL MBPs were added into 200 μL of 500 nM "Y"-CP and rotated gently for 2 h at room temperature for the hybridization reaction. After that, the free un-reacted "Y"-CP was separated from the final MCPs by a controllable magnetic field. The MCPs were then washed with the hybridization buffer three times to remove the non-hybridized components, and re-suspended in a final volume of 100 μL of hybridization buffer, and stored at 4 °C.

2.5. Fabrication of the fluorescence biosensor and long DNA sequence analysis

Initially, MoS_2 solution was ultrasonicated for 1 h in deionized water to obtain better dispersed nanosheets. Next, 50 μL of 1 μM FAM-labeled probe was added into 50 μL of 22 μg mL^{-1} MoS_2 nanosheets solution. The whole was fully mixed for 20 min at room temperature to quench the fluorophore due to the ssDNA being firmly adsorbed on the surface of the MoS_2 nanosheets, attributed to the strong π–π stacking interaction.

The MCPs were first separated from the 100 μL resuspended solution, leaving as a wet cake on the container wall. Subsequently, 1000 μL of various concentrations of the long DNA target with stem loop structures was added to the EP tube containing the MCPs. Then the mixture was rotated gently for 2 h at room temperature to capture the target, followed by magnetically extracting the MCP@target to remove the unreacted components and the matrix. Next, 100 μL of 1 μM assistant sequence was mixed with the MCP@target, and the displacement reaction was performed for 30 min at room temperature, followed by magnetically separating the "Y"-CP@target and MBP@assistant sequence, leaving the "Y"-CP@target in the supernatant. Then, 50 μL "Y"-CP@target solution was added into 50 μL MoS_2@FAM-labeled probe solution for 20 min at room temperature. Finally, the fluorescence emission spectrum was determined in the wavelength range of 500–650 nm with an excitation wavelength of 495 nm. Both the silt widths of excitation and emission were 5 nm, and the voltage was 700 V. The difference in fluorescence intensity at 515 nm was employed to calculate the concentration of the target. After that, the MBPs could be regenerated by magnetically separating and aspirating the supernatant at 95 °C for 5 min.

2.6. Gel electrophoresis

The feasibility of the "Y"-CP-actuated capture and separation of long DNA target was analyzed by 2% agarose gel electrophoresis. The gel was run at 120 V for 26 min in 1× TBE buffer (Tris/boric acid/EDTA, pH 7.4). The image of the electrophoresis was recorded with a Bio-Rad digital system.

2.7. Circular dichroism spectra

Here, 10 μL of 10 μM long target sample was dissolved in hybridization buffer to achieve 200 μL of a 250 nM sample concentration. The short target sample containing the exposed fusion site after forming the "Y"-CP@target was synthesized and prepared to achieve the same concentration as for the long target sample. The circular dichroism (CD) spectra were recorded in triplicate in the 220–350 nm range with a 1 nm data interval and 100 nm min^{-1} data collection rate. The buffer spectrum was subtracted from the sample spectrum.

2.8. Ultraviolet absorbance experiment for the MoS_2 nanosheets and FAM

First, 9.40×10^{-3} g FAM solid was dissolved in 0.5 mL dimethyl sulfoxide, and then the hybridization buffer was added to achieve a 1×10^{-6} mol L^{-1} FAM sample concentration. Subsequently, 100 μL MoS_2 nanosheets solution was mixed with an equal volume of hybridization buffer and FAM sample for 20 min, respectively. Then, the UV absorption spectra of the two samples were detected by using a UV-visible spectrophotometer.

3. Results and discussion

3.1. Design principle of the biosensor

The principle for the "Y"-junction-nanostructure to unlock the stem loop structure of the PML/RARα DNA "L" subtype is shown in Fig. S1.† Long sequence PML/RARα DNA "L" subtype with the sequence of 5′-CCCAACAGCAACCACGTGGCCAGTGGCGCCGGGGAGGCAGCCATTGAGACCCAGAGCAGCAGTTCTGAAGAGATAGTGCCCAGCCCTCCCTCGCCACCCC-3′ could form stem loop structures, one of which blocked the fusion site (italic and underlined base sequence portions), resulting in the failure of hybridization between the specific probe and the target. Meanwhile, the smart "Y"-CP self-assembled by RARα-probe (green portion) with the sequence of the 5′-CACTATCTCTTCAGAACTTTTTGTCTCAAGCTTATGAAATGAACTCAAGGTACG-3′ and PML-probe (red portion) with the sequence of 5′-TTCATAAGCTTGAGACAATTCACTGGCCACGTGGTTGC-3′ contained two symmetric single-stranded overhangs complementary to the target DNA. The overhang (a portion) belonging to the PML-probe could invade and destroy the thermal stability of the stem loop by the toehold-mediated strand displacement reaction, exposing the blocked fusion site (italic base sequence portions). The purpose of the overhang belonging to the RARα-probe was to further reduce the formation risk of extra secondary structures and locking the detection region for the subsequent hybridization reaction. After specific binding, the long target was transformed into a short target for easy detection based on a conformational change of the nucleic acids sequence. Thus, the "Y"-CP could provide the prerequisite for achieving the specific fragment hybridization detection of long nucleic acids.

Based on the above principle, the scheme for the fluorescence biosensor for PML/RARα DNA "L" subtype detection is shown in Scheme 1. Initially, as illustrated in Scheme 1B, considering that layered MoS_2 could adsorb the FAM-labeled single-stranded probe (sequence: 5′-FAM-TGGGTCTCAATGGCTGCCTCCCC-3′) *via* van der Waals interactions and effectively quench the fluorophore labeled at the end of absorbed single-stranded nucleic acids *via* FRET, a MoS_2@FAM-probe biosensor was developed for one-step nucleic acids detection. Then, as shown in Scheme 1A, the Linker DNA was anchored on magnetic beads by amide reaction to further assemble the "Y"-CP onto its surface by sequence hybridization, and the resultant MCP was employed for the stable capture and enrichment of the target. In the presence of the target, once the

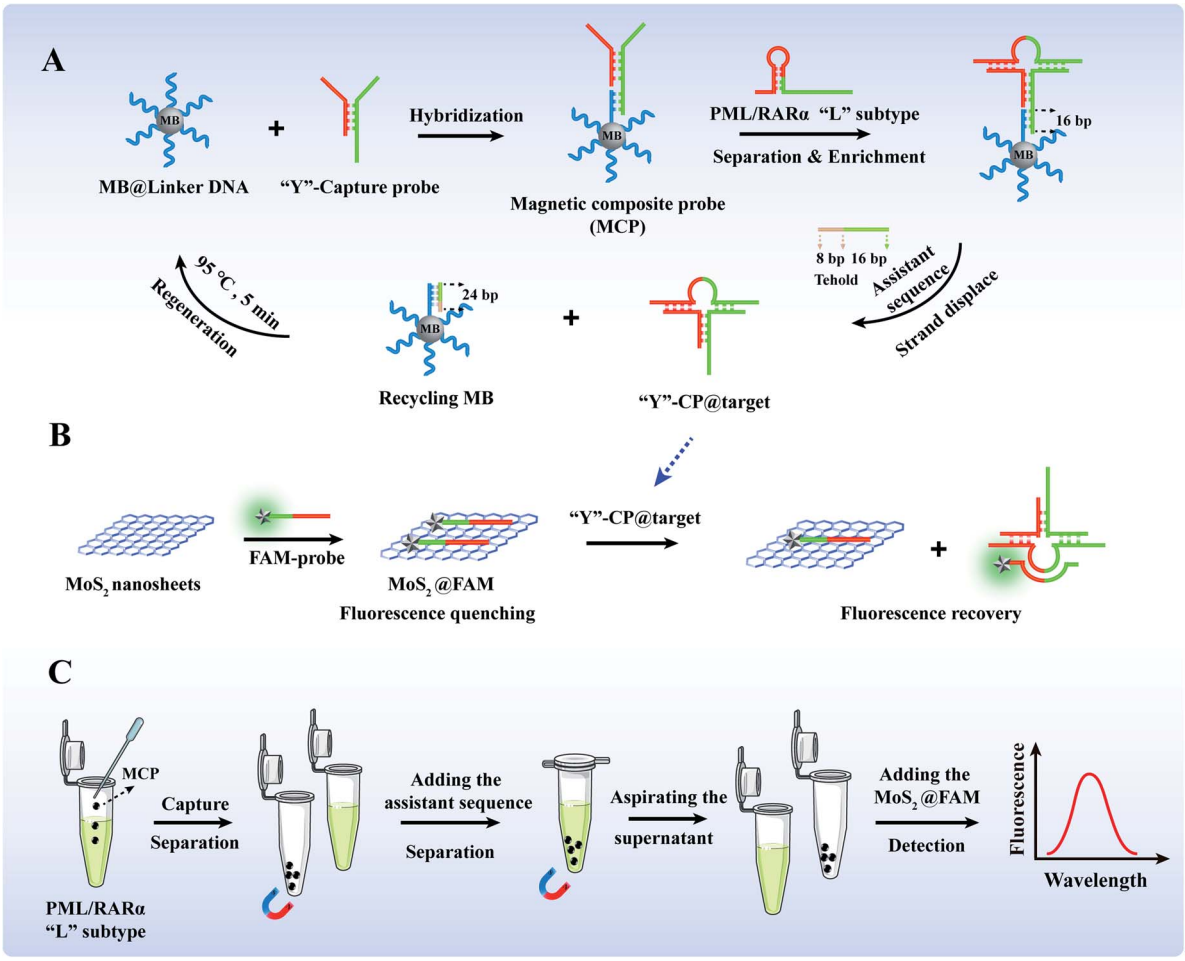

Scheme 1 Schematic illustration of the "off–on" MoS_2@FAM-probe biosensor for long PML/RARα DNA "L" subtype detection by integrating MCP-actuated recognition, deblocking, and extraction of the target. (A) Recognition and conversion of PML/RARα DNA "L" subtype. (B) Fluorescence signal output based on MoS_2@FAM-labeled probe biosensor. (C) The procedure of sample testing.

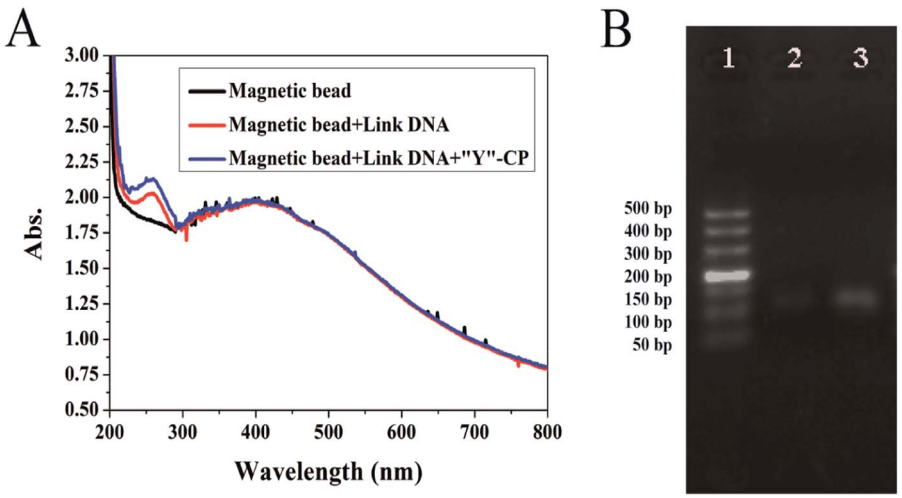

Fig. 1 (A) UV-vis absorption of MBs, MBPs, MCPs suspensions. Before (black curve) and after (red curve) Linker DNA incubation with MBs; after "Y"-CP incubation with MBPs (blue curve). (B) Gel electrophoresis analysis of "Y"-CP concentration in the samples from before (Lane 3) and after (Land 2) "Y"-CP incubation with MBPs, Land 1: DL 500 DNA ladder marker.

MCP specifically recognized and bound the PML/RARα DNA "L" subtype, its hairpin was opened and the fusion region was exposed. Subsequently, with the addition of assistant sequence, the "Y"-CP@target was separated from MBP by a toehold-mediated strand displacement reaction, thus leaving the captured target in the supernatant after magnetic separation. This was followed by adding "Y"-CP@target into the MoS_2@FAM-probe solution, whereby the "Y"-CP@target/FAM-probe formed by fusion region specific hybridization could not be effectively adsorbed because the affinity of the MoS_2 nanosheets to dsDNA was relatively low. As a result, a strong analytical signal was obtained based on the fluorescence quenching–restoration behavior. In addition, economically, the MBP could be regenerated for recycling. Scheme 1C shows the operation protocol for the assay, whereby, as expected, the magnetic separation not only achieved enrichment of the target, but also effectively avoided the interference of the matrix on the fluorescence signal. Therefore, the developed strategy exhibited its potential for the sensitive and accurate detection of PML/RARα DNA "L" subtype by blocking the fusion site without signal amplification.

3.2. Characterization of the MCP and MoS_2 nanosheets

To verify that the Linker DNA was bound to the MBs, the UV-vis absorptions of MBs and MBPs suspension were measured before and after Linker DNA conjugation to the MBs due to the characteristic absorption peak of DNA at 260 nm. As shown in Fig. 1A, the characteristic absorption peaks of nucleic acids appeared after the Linker DNA coupling with the MBs at 260 nm (red curve), indicating that the Linker DNA successfully was bound to the MBs. Then, to further investigate the formation ability of the MCPs, the UV-vis absorption of the MCPs suspension was measured after "Y"-CP conjugation to the MBPs. As shown in Fig. 1A, the absorption peaks of nucleic acids from MCPs was higher than that from the MBPs at 260 nm (blue curve), indicating that "Y"-CP was successfully bound to the MBPs. Simultaneously, the gel electrophoresis analysis of the "Y"-CP concentration was performed before and after the specific hybridization between the MBPs and "Y"-CP. The electrophoresis samples before and after the reaction consisted of "Y"-CP solution and the hybridization buffer (1 : 1), the supernatant after magnetic separation, and the MCPs rinsed buffer (removing the nonspecific adsorption) (1 : 1), respectively, which had equal volumes. As shown in Fig. 1B, the band of Lane 2 (after hybridization) was thinner than the band of Lane 3 (before hybridization). Then, the gray-scale values of the two bands were analyzed by using Image Lab 3.0. As shown in Fig. S2,† the gray-scale mean values were 652 (Lane 2) and 1103 (Lane 3), indicating about 40% "Y"-CP was bound to MBPs. The electrophoresis results were in agreement with the change un UV-vis absorption, proving MCP could be successfully constructed based on the designed assembly process.

Typical AFM and TEM images of the MoS_2 nanosheets are depicted in Fig. 2A and B respectively, which exhibited the morphology of the MoS_2 nanosheets with a mean thickness of 0.9 ± 0.2 nm and diameter of 213.5 ± 3.8 nm. The morphology of the MoS_2 nanosheets was also surveyed by SEM (Fig. 2C), where it could be seen that the as-prepared MoS_2 nanosheets had an average diameter of 212 ± 3.4 nm, which was in agreement with the TEM results. The synthetic MoS_2 suspension (Fig. 2D, inset) was brown. Also, the UV-vis spectrum is shown in Fig. 2D, where two characteristic absorption peaks of MoS_2 nanosheets could be seen located at around 610–690 nm, which was in agreement with the reported work,[28,32] indicating the existence of MoS_2 nanosheets in the dispersed solvent. Based on the Lambert–Beer law, the concentration of the MoS_2 nanosheets solution was calculated to be 22.19 μg mL^{-1} (extinction coefficient = 3400 mL mg^{-1} m^{-1} at 670 nm).[24,28]

3.3. Comparison of the ultraviolet spectra of the MoS_2 solution and MoS_2 + FAM solution

To rule out other fluorescence quenching mechanisms beside FRET between FAM and MoS_2 nanosheets, we assumed that FAM and MoS_2 nanosheets could form compounds or take part

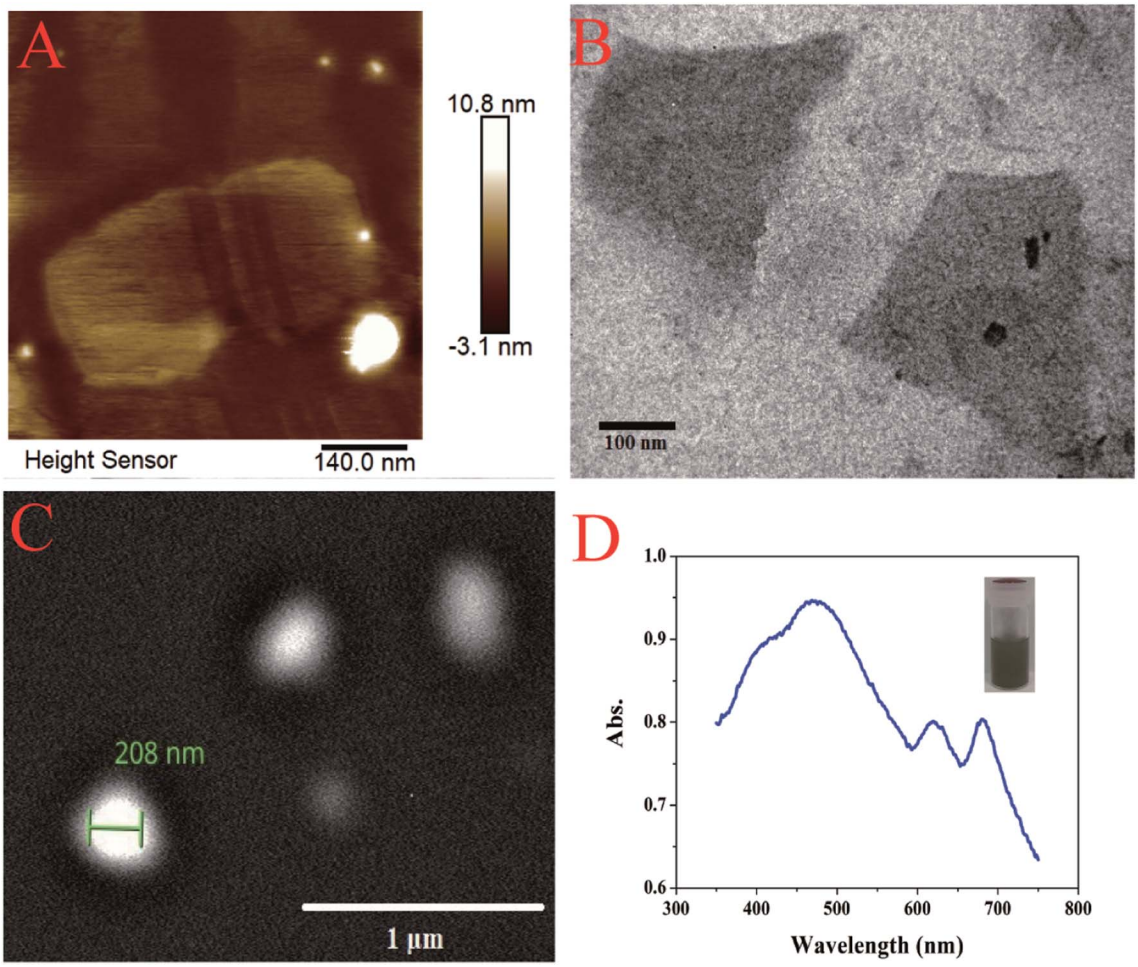

Fig. 2 (A) AFM images of the MoS_2 nanosheets with 140 nm scale. (B) TEM images of the MoS_2 nanosheets with 100 nm scale. (C) SEM images of MoS_2 nanosheets with 1 μm scale. (D) UV-vis spectrum of MoS_2 nanosheets. Inset: photograph of the MoS_2 nanosheets suspension.

in electron transfer. In this case, the UV absorption spectrum position of MoS_2 nanosheets could shift, or a new absorption peak of MoS_2 nanosheets could appear after adding FAM into MoS_2 solution. However, as shown in Fig. S3,† the UV absorption spectra of the MoS_2 nanosheets were consistent before and after the addition of FAM. Therefore, the results demonstrated that there had not been the formation of compounds and electron transfer had not occurred between FAM and MoS_2, which ruled out the fluorescence quenching mechanism caused by electron transfer and by the formation of nonfluorescent compounds between FAM and MoS_2 nanosheets.

3.4. Feasibility of the biosensing strategy

To confirm the deblocking function of "Y"-CP, the CD spectra were used to determine the possible changes in the stem loop structure of the long nucleic acids triggered through "Y"-CP. As shown in Fig. S4,† the CD spectra pattern for the long target with stem loop structures was characterized by a peak at around 270 nm, and a valley in the 310–320 nm wavelength range (black curve), which was similar to the reported work.[36] By contrast, the CD spectra for the short target with an exposed fusion site showed no characteristic peak or valley (red curve), indicating that "Y"-CP really unlocked the stem loop structures of the long nucleic acids target and could achieve the exposure of the fusion site.

In order to confirm whether the Linker DNA@"Y"-CP and assistant sequence-actuated work worked as expected, the hybridization products of the reaction system were characterized by gel electrophoresis. As shown in Fig. 3A, with the hybridization of the PML probe and RARα probe, the clear band exhibited the efficient "Y" assembly products in Lane 2. Lane 3 was loaded with the mixture of Linker DNA and "Y"-CP, which exhibited a lower mobility compared to Lane 2. The hybridization products after "Y"-CP@Linker DNA conjugation to the long DNA target gave a more obvious macromolecule band compared to that of the single "Y"-CP and "Y"-CP@Linker DNA in Lane 4. After further addition of the assistant sequence, the Linker DNA was successfully separated from the "Y"-CP@long DNA target in Lane 5. These results demonstrated the programmed assembly protocol worked, as anticipated.

To further confirm the key role of "Y"-CP in signal "off–on" switching and the validity of the biosensor, the fluorescence emission spectra of MoS_2@FAM-probe biosensor were explored

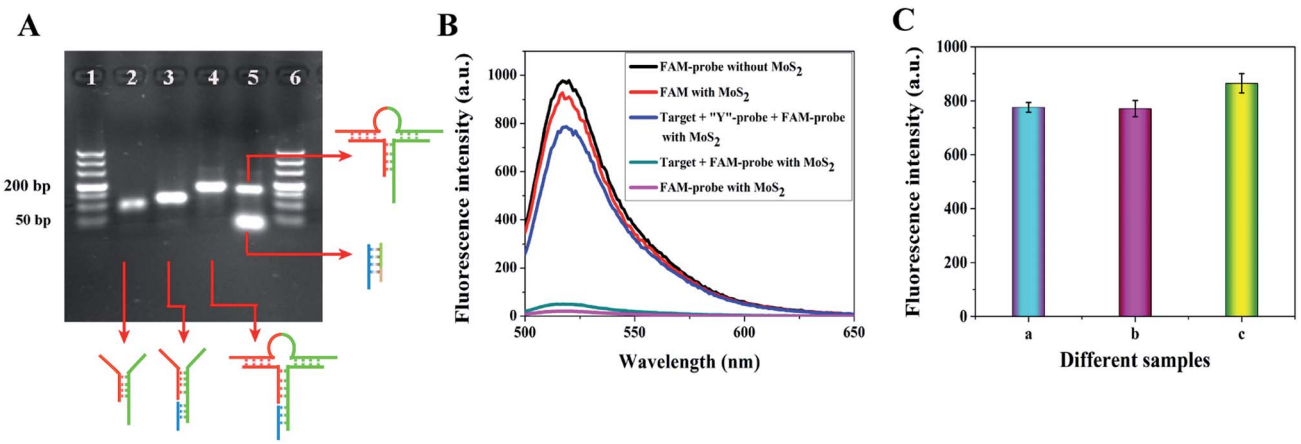

Fig. 3 (A) 2% agarose gel electrophoretic characterization of the hybridization products of the reaction system. Lane 1 and 6: DL 500 DNA ladder marker; Lane 2: "Y"-CP (PML probe + RARα probe); Lane 3: Linker DNA + "Y"-CP; Lane 4: Linker DNA + "Y"-CP + target; Lane 5: Linker DNA@assistant sequence and "Y"-CP@long DNA target. (B) Fluorescence emission spectra of FAM without MoS_2 nanosheets (black curve), FAM with MoS_2 nanosheets (red curve), target + FAM-probe with MoS_2 nanosheets (green curve), and target@"Y"-CP + FAM-probe with MoS_2 nanosheets (blue curve). Negative control (purple curve). (C) Fluorescence signals based on Sample A, Sample B, and Sample C. Error bar represents the standard deviation ($n = 3$).

in the presence and absence of "Y"-CP, respectively. As shown in Fig. 3B, in order to prove that MoS_2 nanosheets had no quenching effect on FAM in the absence of single stranded nucleic acid, we mixed FAM with MoS_2 nanosheets and carried out fluorescence detection. The results showed that there was no significant signal change compared with the fluorescence signal based on FAM without MoS_2 (curve black, red). This experiment further confirmed the feasibility of our methodology. Then, the FAM without MoS_2 and FAM with MoS_2 were employed as positive controls in the experiment. First, the two positive controls (curve black, red) obtained high signals, which indicated the effectiveness of the testing process. Second, it could be clearly observed that the pure long DNA target with the stem loop structure had a very low fluorescence intensity owing to its inability to effectively crosslink with the FAM-probe absorbed on MoS_2 (curve green). By contrast, the signal of the "Y"-CP@long DNA target (curve blue) was about 18 times that of the pure long target due to the fluorescence restoration behavior mediated by the double-stranded DNA formation. The purple curve represents the negative control in the experiment. All the above facts suggested that the "Y"-CP worked as expected.

The fluorescence biosensing system might be interfered with by the matrix in serum. To verify the accuracy of the detection results after magnetic separation of the serum specimen, the fluorescence detection results of the MoS_2@FAM-probe biosensing system were examined with three different test samples with the same concentration of target. The matrix of Sample A was a hybridization buffer, representing the case with no serum matrix interference throughout the experiment. Thus, Sample A acted as the control. The original matrix of Sample B was serum; however, the serum matrix was displaced by hybridization buffer after magnetic separation, which represented the case where there was no serum matrix interference in the fluorescence detection stage. The matrix of Sample C remained as serum in the fluorescence analysis stage, representing the case with the presence of serum matrix interference in the process of signal detection. As shown in Fig. 3C, the fluorescence signal from testing Sample B showed almost no difference with the signal from testing Sample A, while the fluorescence signal of testing Sample C was higher than the fluorescence signal of Samples B and A, indicating that the serum matrix probably promoted the non-specific fluorescence signals. Therefore, these results demonstrated the biosensing strategy could effectively eliminate the matrix interference based on magnetic separation to ensure the accuracy of the detection results in serum specimens.

3.5. Optimization of the experimental conditions

In order to achieve the perfect construction of MCPs and the highly efficient detection of the target, crucial experimental variables were investigated to attain the optimal sensing performance. The coverage of the "Y"-CP on the MBPs surface had a great influence on the capture efficiency of MCPs; thus, the ratio of "Y"-CP and MBPs was first optimized. As shown in Fig. S5A,† four different proportions of "Y"-CP to MBPs were explored. While 2 times "Y"-CP to MBPs achieved the maximum signal-to-noise ratio, a higher ratio of "Y"-CP on the MBPs surface did not continue to increase the signal output. Thus, a 2 : 1 ratio of "Y"-CP to MBPs was selected for the further experiments. According to the calculation based on the working concentration of MBPs and "Y"-CP, 200 μL of "Y"-CP (500 nM) was added into 100 μL MBPs (0.4 mg mL^{-1}), which could obtain the perfect MCPs.

Since the fluorescence signal from the "off–on" switching induced by MoS_2 nanosheets served as the analytical signal in this work, it was crucial to determine the appropriate concentration of MoS_2 nanosheets to obtain the best analysis performance. Thus, five concentrations of MoS_2 nanosheets were

explored in this experiment. As shown in Fig. S5B,† it could be clearly observed that the noise decreased gradually with the increasing concentration of MoS_2 nanosheets due to the increase in the fluorescence quenching effect. However, when the concentration of MoS_2 nanosheets was over 11 μg mL^{-1}, the analytical signal started to decrease due to producing an excessive quenching effect, resulting in the quenching of the double-stranded DNA-labeled fluorophores. Thus, 11 μg mL^{-1} of MoS_2 nanosheets was selected as the fluorescence quencher in this work with the maximum signal-to-noise ratio.

In addition, to further determine the appropriate hybridization time between the FAM-labeled probe and the "Y"-CP@long DNA target, the reaction time was optimized. As shown in Fig. S5C,† the signal-to-noise ratio increased with the prolonged reaction time and plateaued at 20 min, indicating that the reaction between the FAM-labeled probe and the "Y"-CP@long DNA target had reached equilibrium. As a consequence, 20 min was chosen as the optimal reaction time.

3.6. Sensitivity and specificity of the biosensor

Under the respective optimal reaction conditions, we investigated the detection sensitivity of the biosensing method to the target of long PML/RARα "L" subtype DNA. As exhibited in Fig. 4A, the elevated target concentrations led to a proportional increase in the fluorescence response signal. The plots of the fluorescence signal *vs.* the logarithm of long PML/RARα DNA concentrations showed a strong linear relationship in the range from 1 pM to 200 nM (Fig. 4B). The resulting linear equation is $Y = 123.71 \times \lg c$ (pM) + 39.68 with a correlation coefficient of 0.9983. Based on the 3σ rule, the limit of detection (LOD) for the target was calculated to be 0.223 pM. The data of analytical sensitivity was compared with different assays for the detection of PML/RARα (Table 1), and indicated that this developed method had a better linear range or sensitivity in the case of being amplification-free. Of course, in consideration of the low abundance of the target in real samples, this method could also be combined with appropriate signal amplification technology to further improve the sensitivity of detection.

Moreover, the specificity of the biosensor was evaluated for long DNA targets with stem loop structures by testing the long PML/RARα DNA ("L" subtypes) and four non-targets, including long PML DNA, long RARα DNA, and long PML/RARα DNA of different subtypes ("S" and "V" subtypes) (secondary structure of non-targets shown in Fig. S6–S9†). The hybridization buffer as the control was simultaneously tested under the same experimental conditions. As shown in Fig. 5, the signal of the long PML/RARα DNA "L" subtype was significantly higher than for the non-targets and control, indicating the remarkable specificity of the biosensor. These results clearly showed that the detection system only obtained a low background signal with non-targets. On the contrary, when the target appeared, the developed method could obtain a significant enhancement of the fluorescence signal due to the specific recognition, enrichment, and good signal response of the biosensing strategy. Based on the above results, this method demonstrated good analytical performance and has potential value in the specific detection of long nucleic acids from real samples.

3.7. Selectivity, stability, repeatability, reproducibility, and reusability of the strategy

Three DNA mismatch (a portion) PML/RARα "L" subtype DNA samples were used to evaluate the selectivity of the assay, including single-base mismatch (SM), three-bases mismatch (TM), non-complementary DNA (NC). Also, one two-bases mismatch (TWM) (RARα portion) PML/RARα "L" subtype was also used to evaluate the stability of assay. A short target was employed as a positive control in the experiment. As shown in Fig. S10,† the fluorescence signal of target DNA at 1 nM was about 3 times that of SM and 10 times that of TM, and the signal from NC was similar to that for the blank. On the contrary, TWM obtained almost an equal fluorescence signal with that of the target DNA. These results showed that this method displayed good selectivity and stability.

Repeatability and reproducibility, which are two important analytical parameters of the method, were further studied by the intra-assay and inter-assay imprecision, which were

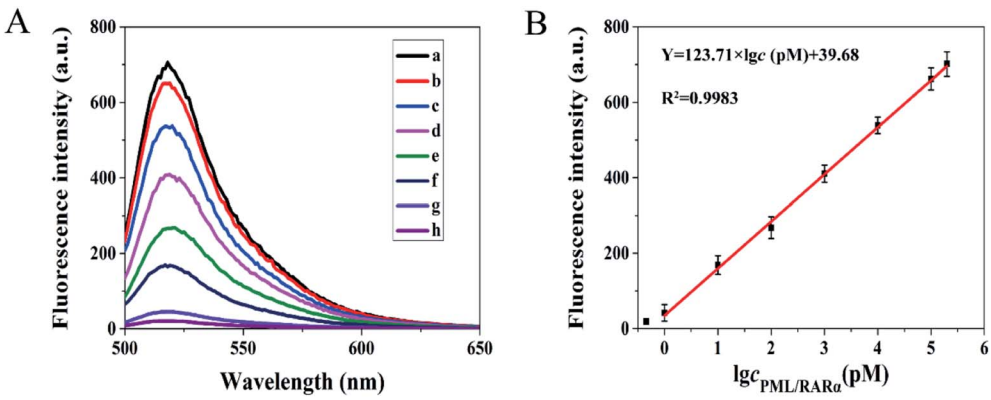

Fig. 4 (A) Fluorescence emission spectra for the detection of PML/RARα DNA "L" subtype at 2×10^5, 1×10^5, 1×10^4, 1×10^3, 1×10^2, 10, 1, 0 pM (from a to h). (B) Calibration plots of the fluorescence signals *vs.* the logarithm of PML/RARα DNA "L" subtype concentrations from 1 pM to 200 nM. Error bar represents the standard deviation ($n = 3$).

Table 1 Comparison of different methods for PML/RARα DNA detection

Target	Strategy	Dynamic range	LOD	Reference
PML/RARα	Enzyme-amplified electrochemical biosensor	1 pM to 100 nM	83 fM	37
PML/RARα	Gold electrode electrochemical biosensor	60 pM to 220 pM	6.7 pM	38
PML/RARα	Sequence-specific electrochemical biosensor	500 pM to 10 nM	1 pM	39
PML/RARα	MoS_2@FAM-probe biosensor based on MCP	1 pM to 200 nM	223 fM	This work

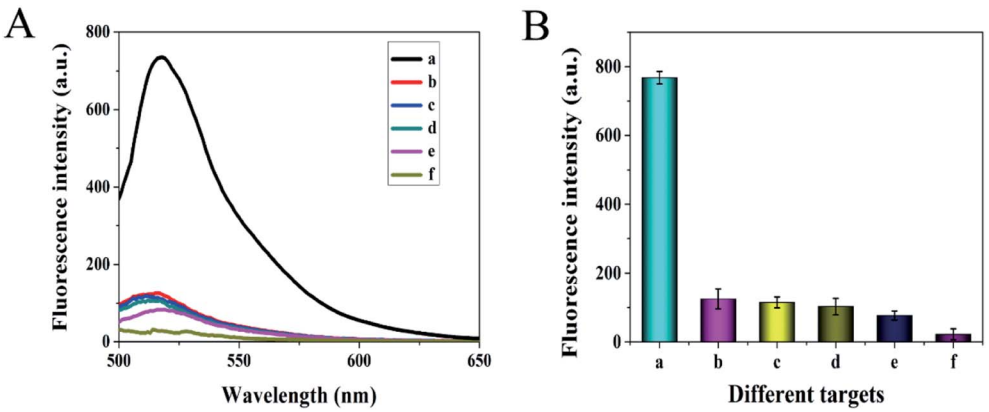

Fig. 5 Fluorescence emission spectra (A) and fluorescence response signals (B) for specificity of PML/RARα detection against PML/RARα DNA "L" subtype (a) and different non-targets: RARα DNA (b), PML/RARα DNA "S" subtype (c), PML DNA (d), PML/RARα DNA "V" subtype (e), blank (f). Error bar represents the standard deviation ($n = 3$).

investigated five times with 10 nM target in one batch and in five different batches of MCPs and MoS_2@FAM-probes, respectively. As shown in Table S2,† the coefficient of variation (CV) and relative standard deviation (RSD) analyzed from the intra-assay were 1.05% and 5.72%, respectively. The CV and RSD analyzed from the inter-assay were 1.31% and 7.07%, respectively. These results indicated this biosensing system had acceptable repeatability and reproducibility.

Furthermore, the reusability of the MBPs was explored in regeneration experiments performed on the same batch MBPs. Taking a CV less than 5% as an acceptable result, after 40 times regenerations, the fluorescence signal of 100 nM target retained 95.1% of the original signal (619 : 651), indicating the MBPs could be reused with great analytical performance and the biosensing strategy had good cost-efficiency.

3.8. Real samples

To evaluate the reliability of the method in a relatively complex matrix serum sample, three different concentrations of samples for recovery experiments were prepared by adding synthetic PML/RARα DNA "L" subtype into serum samples containing 1 mg mL^{-1} salmon sperm DNA. From Table S3,† it can be seen that the recoveries varied from 98.6% to 105%, which proved that the developed protocol could indeed eliminate the matrix effect. The high accuracy resulted from the efficient extraction and enrichment of the target, avoiding the interference of the serum protein on fluorescence detection. Therefore, the method offered a new insight into sensitively and selectively detecting long DNA strands with secondary structures in real serum samples, in favor of the detection of circulating tumor DNA from serum.

4. Conclusions

In summary, the specific "Y"-Capture Probe ("Y"-CP) was first applied to unlock the stem loop structure of the PML/RARα DNA "L" subtype *via* triggering conformational change of the nucleic acids in this work. As a result, an "off–on" MoS_2@FAM-labeled probe biosensor was successfully developed for the specific fragments analysis of long nucleic acids with secondary structures in human serum samples by using an MCP-actuated reactor. This biosensing method could effectively eliminate the obstacles associated with conformation hindrance and achieved target separation, making feasible direct hybridization detection of specific fragments in long nucleic acids based on nanomaterial interface. Most importantly, the protocol for 100 bases PML/RARα DNA "L" subtype detection exhibited outstanding sensitivity, specificity, a low matrix effect, and good stability without intricate amplification, demonstrating the strategy is promising to achieve the simple and rapid liquid biopsy of nucleic acids. As a future direction, the present assay provides a potential strategy for the detection of long nucleic acids from ctDNA and ctRNA.

However, some issues need to be further studied. First, there may be longer nucleic acid chains and more complex chains of hierarchical conformations in real samples. Therefore, a probe with more stability and efficiency needs to be precisely designed, avoiding any interference from irrelevant conformations and ensuring the accurate detection. Second, if base

mutation occurs in the binding site between the nucleic acid and probe, that would reduce the work-efficiency of the probe. Thus, the combined application of dual-probes or multi-probes may be a consideration, which would not only improve the detection efficiency of long nucleic acids, but would also offer a chance for the identification of mutant sites. Overall, the fabricated biosensing strategy is a valid approach, which is worth further exploration.

Conflicts of interest

The authors have declared that no conflicting interests exist.

Acknowledgements

This work was supported by the National Natural Science Foundation of China (81873980, 81873972 and 21804015), the Special Project for Social Livelihood and Technological Innovation of Chongqing (cstc2016shmszx130043), Science and Technology Project of Sichuan (2019YJ0392), Science and Technology Project of Nanchong (18SXHZ0512), Doctor foundation of North Sichuan Medical College (CBY19-QD01).

References

1 C. T. Lin and T. Ha, *Methods Mol. Biol.*, 2017, **1486**, 295–316.
2 N. Jiang, J. Pan, S. Fang, C. Zhou, Y. Han, J. Chen, X. Meng, X. Jin and Z. Gong, *Clin. Chim. Acta*, 2019, **19**, 31841–31848.
3 S. Dahariya, I. Paddibhatla, S. Kumar, S. Raghuwanshi, A. Pallepati and R. K. Gutti, *Mol. Immunol.*, 2019, **112**, 82–92.
4 A. L. Volckmar, H. Sültmann, A. Riediger, T. Fioretos, P. Schirmacher, V. Endris, A. Stenzinger and S. Dietz, *Genes, Chromosomes Cancer*, 2018, **57**, 123–139.
5 Y. Yao, Y. Liu, H. Zhang and X. Wang, *Methods Appl. Fluoresc.*, 2019, **7**, 035006.
6 L. Guo, Y. Xu, A. R. Ferhan, G. Chen and D. H. Kim, *J. Am. Chem. Soc.*, 2013, **135**, 12338–12345.
7 Y. Hu, L. Zhang, Y. Zhang, B. Wang, Y. Wang, Q. Fan, W. Huang and L. Wang, *ACS Appl. Mater. Interfaces*, 2015, **7**, 2459–2466.
8 H. R. Underhill, J. O. Kitzman, S. Hellwig, N. C. Welker, R. Daza, D. N. Baker, K. M. Gligorich, R. C. Rostomily, M. P. Bronner and J. Shendure, *PLoS Genet.*, 2016, **12**, e1006162.
9 P. Jiang, C. W. Chan, K. C. Chan, S. H. Cheng, J. Wong, V. W. Wong, G. L. Wong, S. L. Chan, T. S. Mok, H. L. Chan, P. B. Lai, R. W. Chiu and Y. M. Lo, *Proc. Natl. Acad. Sci. U. S. A.*, 2015, **112**, 1317–1325.
10 H. Hata, T. Kitajima and A. Suyama, *Nucleic Acids Res.*, 2018, **46**, 782–791.
11 M. Sanromán-Iglesias, C. H. Lawrie, L. M. Liz-Marzán and M. Grzelczak, *Bioconjugate Chem.*, 2017, **28**, 903–906.
12 M. Ma, H. Zhu, C. Zhang, X. Sun, X. Gao and G. Chen, *Ann. Transl. Med.*, 2015, **3**, 235.
13 Y. Zhang, J. Tu, D. Wang, H. Zhu, S. K. Maity, X. Qu, B. Bogaert, H. Pei and H. Zhang, *Adv. Mater.*, 2018, **30**, e1703658.
14 S. Jiang, F. Hong, H. Hu, H. Yan and Y. Liu, *ACS Nano*, 2017, **11**, 9370–9381.
15 B. Guo, W. Cheng, Y. J. Xu, X. Y. Zhou, X. M. Li, X. J. Ding and S. J. Ding, *Sci. Rep.*, 2017, **7**, 14037.
16 Z. Zhang, C. Zhong, T. Yuan, X. Zhou, M. Zhao, H. Qian, W. Cheng and T. Chen, *Methods Appl. Fluoresc.*, 2018, **6**, 045003.
17 L. He, D. Q. Lu, H. Liang, S. Xie, C. Luo, M. Hu, L. Xu, X. Zhang and W. Tan, *ACS Nano*, 2017, **11**, 4060–4066.
18 B. Guo, B. Wen, W. Cheng, X. Y. Zhou, X. L. Duan, M. Zhao, Q. F. Xia and S. J. Ding, *Biosens. Bioelectron.*, 2018, **112**, 120–126.
19 J. Xiang, X. Pi, X. Chen, L. Xiang, M. Yang, H. Ren, X. Shen, N. Qi and C. Deng, *Biosens. Bioelectron.*, 2017, **96**, 268–274.
20 S. X. Chen, D. Y. Zhang and G. Seelig, *Nat. Chem.*, 2013, **5**, 782–789.
21 G. Wei, J. Yu, J. Wang, P. Gu, D. J. Birch and Y. J. Chen, *Biomed. Opt.*, 2016, **21**, 97001.
22 X. Guo, M. He, K. Nan, H. Yan, B. Chen and B. Hu, *J. Anal. At. Spectrom.*, 2016, **31**, 406–414.
23 H. Yan, Y. Xu, Y. Lu and W. Xing, *Anal. Chem.*, 2017, **89**, 10137–10140.
24 H. B. Wang, Y. Li, H. Y. Bai and Y. M. Liu, *Sens. Actuators, B*, 2018, **259**, 204–210.
25 A. H. Loo, A. Bonanni, A. Ambrosi and M. Pumera, *Nanoscale*, 2014, **6**, 11971–11975.
26 J. Lee, P. Dak, Y. Lee, H. Park, W. Choi, M. A. Alam and S. Kim, *Sci. Rep.*, 2014, **4**, 7352.
27 C. Zhu, Z. Zeng, H. Li, F. Li, C. Fan and H. Zhang, *J. Am. Chem. Soc.*, 2013, **135**, 5998–6001.
28 C. Lu, Y. Liu, Y. Ying and J. Liu, *Langmuir*, 2017, **33**, 630–637.
29 L. Xiao, L. Xu, C. Gao, Y. Zhang, Q. Yao and G. J. Zhang, *Sensors*, 2016, **16**, 1561.
30 I. A. Rahman and A. Purqon, *J. Phys.: Conf. Ser.*, 2017, **877**, 012026.
31 H. M. Deng, X. J. Yang and Z. Q. Gao, *Analyst*, 2015, **140**, 3210–3215.
32 S. Rafiei, M. Dadmehr, M. Hosseini, H. A. Kermani and M. R. Ganjali, *Methods Appl. Fluoresc.*, 2019, **7**, 025001.
33 H. De Thé, C. Chomienne, M. Lanotte, L. Degos and A. Dejean, *Nature*, 1990, **347**, 558–561.
34 Z. Chen and S. J. Chen, *Leuk. Lymphoma*, 1992, **8**, 253–260.
35 K. G. Zhou, N. N. Mao, H. X. Wang, Y. Peng and H. L. Zhang, *Angew. Chem., Int. Ed.*, 2011, **50**, 10839–10842.
36 Z. Jahnz-Wechmann, J. Lisowiec-Wachnicka, G. Framski, J. Kosman, J. Boryski and A. Pasternak, *Bioorg. Chem.*, 2017, **71**, 294–298.
37 L. Lin, Q. Liu, L. Wang, A. Liu, S. Weng, Y. Lei, W. Chen, X. Lin and Y. Chen, *Biosens. Bioelectron.*, 2011, **28**, 277–283.
38 G. Zhong, A. Liu, X. Chen, K. Wang, Z. Lian, Q. Liu, Y. Chen, M. Du and X. Lin, *Biosens. Bioelectron.*, 2011, **26**, 3812–3817.
39 Y. Lei, M. Feng, K. Wang, L. Lin, Y. Chen and X. Lin, *Anal. Bioanal. Chem.*, 2013, **405**, 423–428.

